Solar Energy Materials & Solar Cells 97 (2012) 119–126

Contents lists available at SciVerse ScienceDirect

Solar Energy Materials & Solar Cells

journal homepage: www.elsevier.com/locate/solmat

Optimal geometric design of monolithic thin-film solar modules: Architecture of polymer solar cells

Harald Hoppe [a,*], Marco Seeland [b], Burhan Muhsin [b]

[a] Experimental Physics I, Institute of Physics, Ilmenau University of Technology, Weimarer Street 32, 98693 Ilmenau, Germany
[b] Institute of Physics, Ilmenau University of Technology, Weimarer Street 32, 98693 Ilmenau, Germany

ARTICLE INFO

Available online 13 October 2011

Keywords:
Monolithic solar module
Geometry
Active area
Interconnects
Simulation
Resistive power loss
Diode equation

ABSTRACT

In this study the geometrical optimization of monolithically integrated solar cells into serially connected solar modules is reported. Based on the experimental determination of electrodes′ sheet and intermittent contact resistances, the overall series resistance of individual solar cells and interconnected solar modules is calculated. Taking a constant photocurrent generation density into account, the total Joule respectively resistive power losses are determined by a self-consistent simulation according to the 1-diode model. This method allows optimization of the solar module geometry depending on the material system applied. As an example, polymer solar modules based on ITO-electrodes and ITO-free electrodes were optimized with respect to structuring dimensions.

1. Introduction

Most of today′s thin film solar modules based on inorganic semiconductors employ a semitransparent conducting electrode based on doped metal oxides, named transparent conducting oxides (TCOs) [1]. For example, monolithic solar modules based on amorphous silicon are deposited on Indium doped Tin-Oxide (ITO) or aluminum doped Zink-oxide (Al:ZnO) electrodes on glass. However, one major drawback of these TCOs is the relatively large sheet resistance, as the properties of transparency and conductivity are counterbalancing each other. Hence in general a compromise between doping and layer thickness with respect to the transparency is required. In other words, the limited conductivity of the electrode can cause serious series resistance losses, directly depending on the amount of photogenerated current transported through it [2,3].

Recently, power conversion efficiencies surpassing 8% have been reported for organic solar cells [4,5], making their application in commercial products more and more viable [6]. Aiming for record efficiencies, small scale organic solar cells prepared in research labs are often designed in such way that the impact of the series resistance originating from the TCO is minimized. However, this effect can no longer be neglected when upscaling to practically relevant large-area monolithic solar modules. While many groups have already studied the effect of solar cell length [2,3,7,8] and solar cell geometry [3,9] on overall performance, lesser investigations have been performed on serially interconnected solar cells, respectively solar modules [10,11]. The serial interconnection between adjacent solar cells within the module additionally requires knowledge of the contact resistance between the hole collecting and the electron collecting electrode. Whereas minimizing the solar cell length generally implies better efficiencies for single solar cells, too short solar cell lengths lead to relatively large area losses in case of modules, as the interconnection – i.e. the solar cell distance – becomes a more and more dominant loss factor. In contrast, the application of modern laser ablation techniques [12,13] allows reducing structuring dimensions to levels, where the series resistance across the series connection dominates the overall resistive power losses. Hence a material dependent optimization, balancing between current generation within the cells and series resistance between them, is required in order to maximize the power output of the solar modules.

In this work we exemplarily investigate the design of efficient polymer solar cell based modules using ITO-electrodes or ITO-free electrodes, considering structuring widths down to those levels that are experimentally accessible by laser ablation. While laser ablation is a well established method for inorganic solar modules [14–16], its application to polymer solar cells is currently under development [12,13,17,18].

2. Materials, methods and simulation

2.1. Material system

The standard solar cell structure considered within this report is either based on a semitransparent doped metal oxide electrode

* Corresponding author.
E-mail address: harald.hoppe@tu-ilmenau.de (H. Hoppe).

0927-0248/$ - see front matter © 2011 Elsevier B.V. All rights reserved.
doi:10.1016/j.solmat.2011.09.037

or on a highly conductive doped polyelectrolyte. Both enable sufficient sun light penetration and lateral transport of generated photocurrent. Here, commercial ITO was considered on glass or PET substrates on the one hand, exhibiting different sheet resistances due to different deposition temperatures and resulting crystallinities. On the other hand, highly doped PEDOT:PSS (poly(ethylene-dioxy-thiophene):poly(styrene-sulfonic acid)) (Clevios PH 1000 purchased from H.C. Starck) was applied by solution casting either on glass or on PET. To adapt the work function in case of the ITO-substrates, generally a standard low-conductive PEDOT:PSS layer is solution cast on top of the ITO. Thereupon a blend film of P3HT (poly(3-hexyl-thiophene)) and PCBM (phenyl-C61-butyric-acid-methyl-ester) forms the next layer of the solar cell stack. This layer is generally solution cast on top of the semitransparent electrode. We have demonstrated earlier that this material system is capable of generating photocurrents of 8–10 mA/cm^2 [19,20]. On top of the photoactive layer an opaque aluminum electrode is deposited for efficient extraction of electrons. Using this solar cell structure we have demonstrated power conversion efficiencies of about 3–4% and peak external quantum efficiencies surpassing 60% on ITO-glass [20].

3. Experimental methods

Sheet and contact resistances were determined experimentally with a home built multi-tips setup, using a couple of computer controlled source-measure-units. The sheet resistance R_{sheet} is a size independent magnitude given in the following physical units:

$$[R_{sheet}] = \Omega/\square \tag{1}$$

where $\square$ denotes a square shaped area of the electrode of arbitrary size. Thus the sheet resistance is only depending on the geometry, but not on the size of the area, through which the current is transported.

For determination of the sheet resistance, the four-point probe or the Van der Pauw method was applied [21]. In case of the four-point probe 4 tips are placed equidistantly with separation S on top of the investigated electrode in one line. Then a constant current is injected through the outer two electrodes (1 and 2) and the potential difference is measured between the two inner electrodes (3 and 4); compare with Fig. 1. Due to this arrangement the determined sheet resistance is independent of the contact resistance between the tips and the layer under investigation.

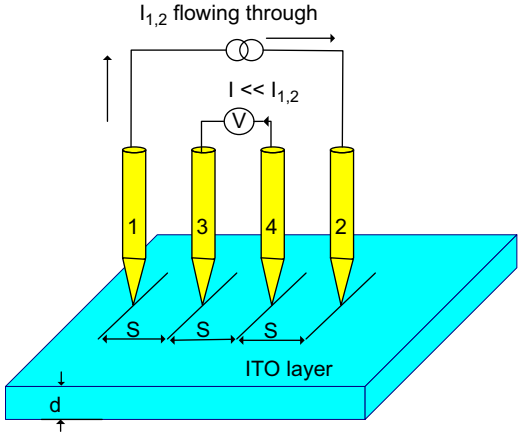

Fig. 1. Schematic description of the four-point-method for determining sheet resistances of an electrode, e.g. the ITO-layer.

Assuming a cylindrical potential distribution within the layer of thickness d yields the electric field

$$E_r = \rho \cdot j = \rho \cdot \frac{I_0}{A} = \rho \cdot \frac{I_0}{2\pi r d}\rho \tag{2}$$

where ρ is the specific resistance, j the current density, I_0 the injected current, A the cylinder area and d the layer thickness. The measured potential U_{34} between tips 3 and 4 then becomes

$$U_{34,E_1} = \int_s^{2s} \vec{E}_1 \cdot d\vec{r} = \frac{\rho I_0}{2\pi d}\int_s^{2s} \frac{1}{r}\cdot d\vec{r}$$

$$U_{34,E_2} = -\frac{\rho I_0}{2\pi d}\int_{2s}^{s} \frac{1}{r}\cdot d\vec{r}$$

$$U_{34} = U_{34,E_1} + U_{34,E_2} = \frac{\rho I_0}{2\pi d}\ln(2) + \frac{\rho I_0}{2\pi d}\ln(2) = \frac{\rho I_0}{\pi d}\ln(2) \tag{3}$$

Solving for the specific resistance leads to

$$\rho = \frac{U_{34}}{I_0}\cdot\frac{\pi d}{\ln(2)} \tag{4}$$

Thus the measurement of the resistance becomes independent of the distance between the tips, and only the layer thickness d remains as dependent variable. In conclusion the layer thickness independent sheet resistance $R_\square$ can be calculated as

$$R_\square = \frac{\rho}{d} \tag{5}$$

The determination of the contact resistance between the electron and the hole extracting electrodes of two adjacent serially connected solar cells is based on the linear transfer length method (TLM) introduced by Shockley in 1964 [22]. As the contact resistance R_C is reciprocally depending on the contact area A_C, an area independent description of the specific contact resistance ρ_C is generally given by

$$\rho_C = R_C \cdot A_C \tag{6}$$

In general, the active part of the contact area, given by $L_T < A_C$, in which the current injected into the contact pads is transferred, has to be distinguished from the geometrical contact area A_C, since the current injected into the contact pad may be confined to a smaller area. However, our measurements on the considered set of electrodes showed that the most accurate description of the specific contact resistance is provided by considering the full geometrical contact area. In the experiment, rectangular contact pads of width w and length S ($A_C = w \cdot S$) were placed under various distances L_n. To eliminate size effects, the contact length S was varied in addition, yielding at least two sets of experiments. The test structure was prepared by pre-structuring the conductive substrate by ditches for electric isolation of the experiments and using a shadow mask for the vapor deposition of the metallic contact pads, as displayed in Fig. 2.

The measurement was performed using a four-point probe design as given in Fig. 3. Between two contact pads of separation L_n a constant current was injected and an additional pair of contacts was used to determine the potential loss across the same structure (compare with Fig. 3).

Repeating the experiment for various contact pad distances L_n yields the total resistance R as a linear function of the distance L_n.

$$R(L_n) = R_{Sheet}\frac{L_n}{w} + 2R_C \tag{7}$$

Extrapolation for $L_n \to 0$ yields twice the pristine contact resistance R_C, as shown in Fig. 4.

Repeating this experiment for different contact pad lengths S allows the determination of the area independent specific contact resistance ρ_C.

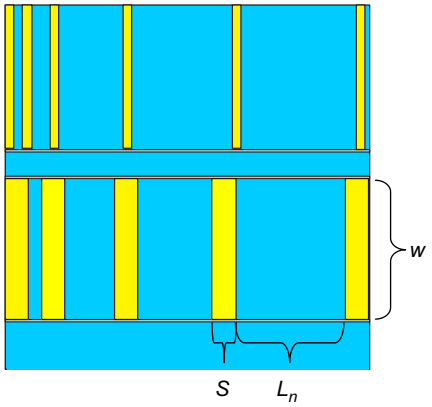

Fig. 2. Structure of the test devices for determination of the specific contact resistance between the electron and hole extracting electrodes. Note that the horizontal lines display ditches that are isolating the two test structures on the common e.g. ITO-substrate from each other.

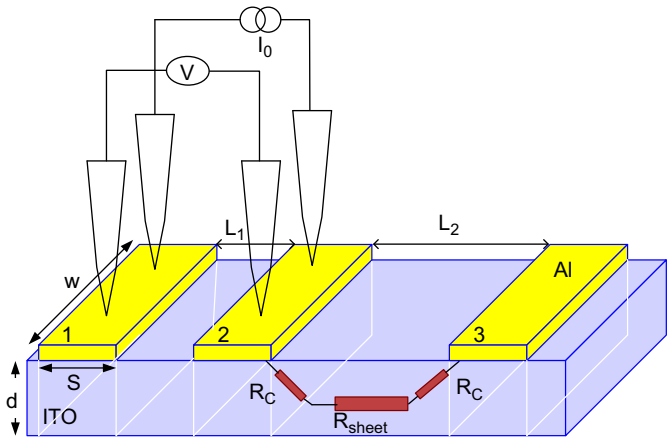

Fig. 3. Measurement of the contact resistance according to the TLM method. Both the contact resistance R_C and the sheet resistance R_{sheet} can be determined simultaneously.

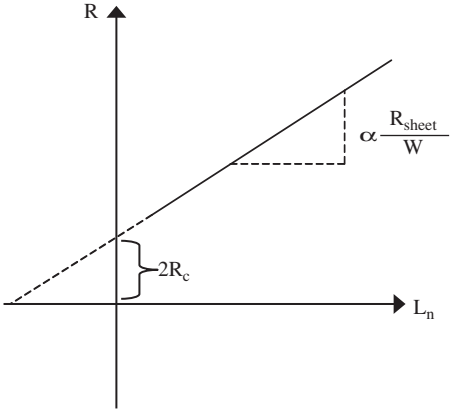

Fig. 4. Determination of the contact resistance R_C using the TLM method under variation of the contact pad distance L_n.

3.1. Simulation

3.1.1. Geometrical power losses

Whereas the power conversion efficiency of solar cells is solely depending on the active area of the device, the module efficiency is determined on the basis of the whole substrate size. As the serial interconnection requires some finite solar cell distance, a simple formula for the power loss due to the photovoltaic inactive area is derived according to Fig. 5.

With that the module efficiency including the geometrical efficiency loss becomes

$$\eta_{module} = \eta_{cell} \cdot \frac{\ell}{\ell + \Delta\ell} \tag{8}$$

where η_{cell} is the power conversion efficiency within the active area of a single cell, l denotes the solar cell length and Δl the solar cell distance within the module. The second factor in Eq. (8) is here referred to as area fill factor of the solar module.

3.1.2. Resistive power losses

In this section individual contributions to dissipative power losses from various ohmic resistances within the photovoltaic module are derived. In Fig. 6 the cross section of a single solar cell–marked with a rectangular dashed line–connected in series within a monolithic solar module is depicted. The solar module may have a certain width w, which is orthogonal to all other dimensions and hence not shown in the schematic.

The arrows in Fig. 6 indicate the direction of the technical current flow within the device. Each current flow is accompanied with a corresponding Joule, respectively, resistive power loss due to the existence of ohmic resistances. Besides some loss occurring within the active layer due to the parallel resistance, five different series resistance contributions are identified and contribute to the total series resistance of the device:

1. the sheet resistance of the aluminum bridge;
2. the sheet resistance of the aluminum electrode above the active area;
3. the sheet resistance of the ITO-electrode below the active area;
4. the sheet resistance of the ITO-bridge;
5. the contact resistance between the ITO and the aluminum.

The series resistance contributions arising from the current transport above or below the active area can be derived as follows:

The photocurrent density J_{photo} is assumed to be constant over the whole solar cell length, thus the laterally transported photocurrent I_{photo} is linearly increasing in the direction of transport within the contacts. At the end of the photoactive region and during the transport of the photocurrent through the electrode bridge, I_{photo} remains constant. Fig. 7 illustrates that for the maximum power point of the device.

In general, the power dissipation within an ohmic resistance is proportional to the current squared passing through it

$$P_{diss} = I^2 \cdot R \tag{9}$$

Considering that each resistance element dR is constant throughout the whole electrode, and that the lateral current $I(x)$ is a function of the position in the direction of transport, the power dissipation becomes

$$d\tilde{P}_{diss}(V) = I(x,V)^2\, dR, \text{ with } dR$$
$$= R_{\square} \frac{dx}{w} \int_0^{P_{diss}} d\tilde{P}_{diss}(V) = \int_{x=0}^{x=\ell} I(x,V)^2 R_{\square} \frac{dx}{w}$$
$$\text{and thus } P_{diss}(V) = I(V)^2 \ell \frac{R_{\square}}{3w}, \text{ with } I(V) = J(V) w \ell. \tag{10}$$

With the help of Eq. (10) we can thus define an effective sheet resistance R_{eff}, which contributes for each electrode to the total series resistance that applies to the passing current

$$R_{eff} = R_{\square} \frac{\ell}{3w}. \tag{11}$$

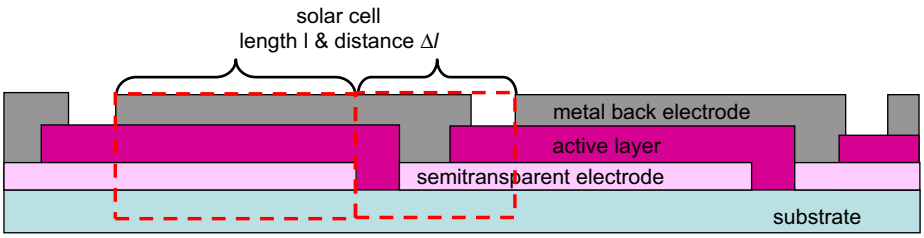

Fig. 5. Illustration of the active area loss for a monolithic solar module with serial interconnection. The solar cell distance Δl represents the region in which no photocurrent generation takes place.

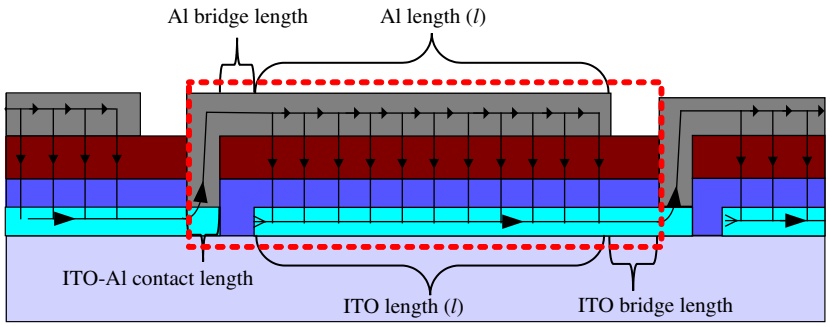

Fig. 6. Schematic cross section of a monolithic solar module with a single serially connected solar cell high-lighted by a rectangular dashed line. Different geometrical lengths of the device resulting in various series resistance contributions are denoted. The arrows indicate the direction of technical current flow within the device.

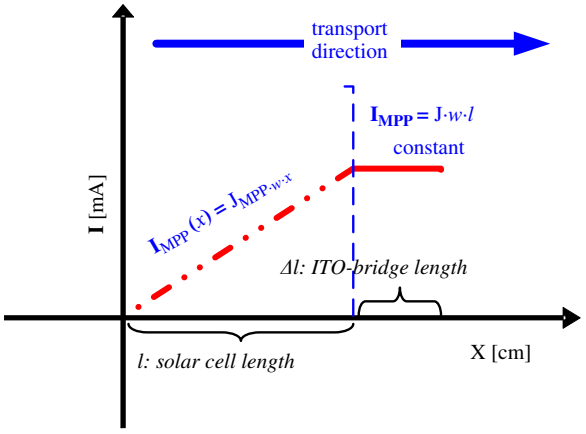

Fig. 7. Current flowing through the ITO-electrode in direction of transport for a solar cell under illumination. Underneath the photoactive layer the current profile rises linearly. This current remains constant for transport over the ITO-bridge towards the ITO-aluminum contact region.

For each electrode bridge the series resistance arising from the sheet resistance calculated geometrically as

$$R_{bridge} = R_{\square}\frac{\ell_{bridge}}{3w_{bridge}} = R_{\square}\frac{\Delta\ell}{3w} \tag{12}$$

where Δl is the solar cell distance, and the bridge length l_{bridge} corresponds by definition to one third of the total solar cell distance. The contact resistance originating from the electrodes contact area simply calculated as

$$R_{contact} = \rho_c\frac{3}{\Delta\ell\cdot w} \tag{13}$$

Finally, the parallel resistance under illumination, responsible for dissipative losses as well, depends only on the active area of each solar cell and calculated as

$$R_P = \rho_P\frac{1}{\ell\cdot w} \tag{14}$$

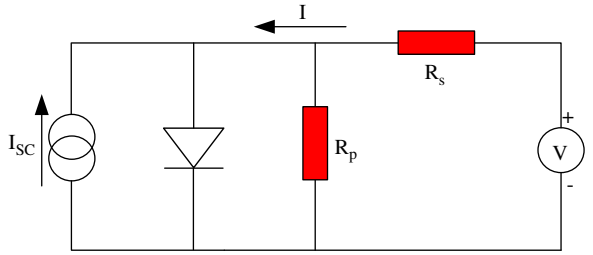

Fig. 8. Equivalent circuit for a solar cell based on the 1-diode model and described by the Shockley equation.

3.2. Self-consistent 1-diode simulation

The self-consistent 1-diode simulation is based on the implicit Shockley equation that is commonly used to describe the current–voltage relationship of solar cells

$$I = I_0\cdot\left\{\exp\left(\frac{e}{nkT}(V-IR_S)\right)-1\right\}+\frac{V-IR_S}{R_P}-I_{SC} \tag{15}$$

with I, I_0 and I_{SC} being the total current, dark saturation current and short circuit photocurrent, respectively, V the voltage, and R_S and R_P being the total series and parallel resistances of each cell. T is the temperature, k the Boltzmann constant, e the elementary charge and n denotes the diode quality factor. The corresponding 1-diode equivalent circuit of a solar cell is given in Fig. 8

At first, all geometrical module parameters as the solar cell length l, width w and solar cell distance Δl are used to calculate the geometry dependent series resistances and the parallel resistance according to the Eqs. (11)–(14). The diode parameters are chosen

independent of the electrodes and are based on the experimentally determined IV-characteristics of P3HT:PCBM solar cells. It is thus assumed that the diode parameters are solely determined by the photoactive layer, which is identical for all devices. This is reasonable, as in all cases aluminum and PEDOT:PSS serve as charge extracting electrodes and hence no differences in the rectification behavior is expected. Neglecting the small differences originating from the solar light propagation through the substrate and the semitransparent electrode, it can be further assumed that the short circuit photocurrent generated by the current source is constant for all cases. Of course this assumption can be removed and the calculation can be refined by conducting optical simulations for each multilayer stack, but this is of minor importance for the effects to be considered here.

Once all equivalent circuit element parameters were determined, the 1-diode simulation was conducted by sweeping the external voltage. Upon determination of all currents passing and voltages resulting at each equivalent circuit element, the global IV-curve was calculated. From the IV-curves all solar cell parameters, i.e. the short circuit photocurrent density J_{SC}, the open circuit voltage V_{OC}, the fill factor FF and the corresponding maximum power point MPP and thus the power conversion efficiency η were determined. Furthermore all resistive power losses were calculated for the involved series and parallel resistances. By considering the active area for power generation alone the geometrical power loss due to the area fill factor (Eq. 7) was implicitly taken into account.

4. Results and discussion

4.1. Resistances

For solar cells based on the P3HT:PCBM material system a constant specific parallel resistance ρ_P under illumination of about 1000 Ω/cm^2 was found experimentally under AM 1.5 solar simulation, independently of the active area of the device. The fit of ρ_P according to $\rho_P = R_P^* A$ for a set of P3HT:PCBM based solar cells with various active areas A is shown in Fig. 9.

The sheet resistances for various electrode materials were determined according to the four-point method (Eqs. 1–5) and are summarized in Table 1.

All specific contact resistances were determined according to the TLM method and are listed for various electrode systems in Table 2. Fig. 10 displays an example for the evaluation of the specific resistance of ITO on glass by fitting the data points for the contact resistances according to Eqs. (7) and (13).

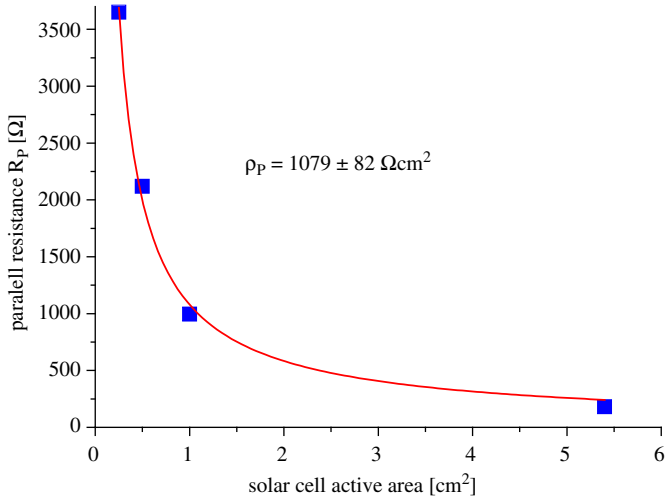

Fig. 9. Experimentally determined parallel resistances under AM 1.5 illumination for solar cells with distinct active areas. The fit according to equation (14) results in a constant specific parallel resistance ρ_P, independent of the solar cell active area.

Table 1
Experimentally determined sheet resistances of various electrode materials.

Material	Layer thickness [nm]	R_{Sheet} [Ω/□]
Aluminum	135	0,16 ± 0,01
ITO on glass	150	12,5 ± 0,6
ITO on PET	150	50 ± 3
PEDOT:PSS PH 1000	150	100 ± 20

Table 2
Experimentally determined specific contact resistances between various semitransparent electrodes and aluminum.

Aluminum vs.	ρ_C [m Ohm cm^2]
ITO on glass	11 ± 1
ITO on PET	17 ± 1
PEDOT:PSS PH 1000	200 ± 20

In the case of PH1000 the achieved film quality critically determined its sheet and contact resistances, which in turn were strongly correlated as well. However, sheet resistances of about 100 Ω/□ and specific contact resistances of 200 m Ohm cm^2 were well reproducible on glass and PET substrates.

Taking all of these experimental results into account, the self-consistent simulation was conducted for a range of solar cell lengths and solar cells distances varying between 0.1 and 2 cm and between 0.01 and 0.5 cm, respectively. Within the calculations it is assumed that the contact length between ITO and aluminum is one-third of the total solar cell distance. The lateral width of the solar cells was fixed to 5 cm in all cases.

For the simulation on ITO–either on glass or on PET–a maximal photocurrent density of 9 mA/cm^2 was used, in good agreement with our earlier experimental results [20]. Due to the stronger absorption occurring in case of the thick PH 1000 electrode, the maximal photocurrent density was reduced to 8 mA/cm^2 without further proof. All diode parameters were kept constant in all cases and were adopted to fit our experimental results obtained on ITO-glass. This restriction is reasonable, as the diode behavior is controlled by the photoactive layer and the charge extracting electrodes, being aluminum and PEDOT:PSS for all cases studied. However, to account for ITO-peaks occurring on rather amorphous ITO deposited on PET, the specific parallel resistance was reduced to half of the value obtained for solar cells on ITO-glass.

At first an overview for the self-consistent 1-diode calculations obtained for polymer solar cells built on ITO-glass is presented.

Fig. 11 displays the power conversion efficiency of a solar cell having a width of 5 cm and a length up to 2 cm and an ITO-bridge length as well as an hole extracting contact length according to 1/3 the cell distance ranging up to 0.5 cm. It is evident that the power conversion efficiency of solar cells is mainly controlled by the cell length and follows closely the behavior of the fill factor (Fig. 11). The fill factor itself is a direct function of the combined power dissipation losses arising from the series resistances and the parallel resistance, both of which are shown in Fig. 12.

The parallel resistance depends only on the inverse solar cell length, whereas the series resistance is depending on both the solar cell length and distance. Fig. 13 displays the plain dependencies of all series resistances on geometric module parameters–as detailed in Eqs. (11)–(13). Though the contact resistance is a hyperbolic and the ITO-bridge resistance is a linear function of the cell distance, the sum of the two is fairly constant for a wide range

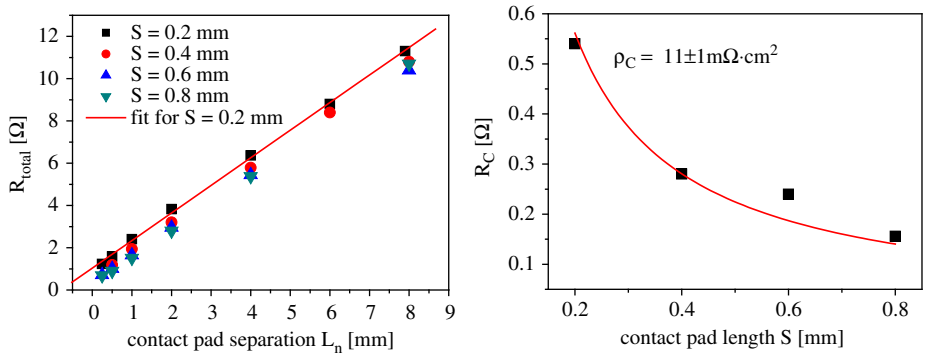

Fig. 10. Fit of the specific contact resistance of ITO on glass (right) to the contact resistances determined experimentally by the TLM method (left) for various contact pad lengths *S*.

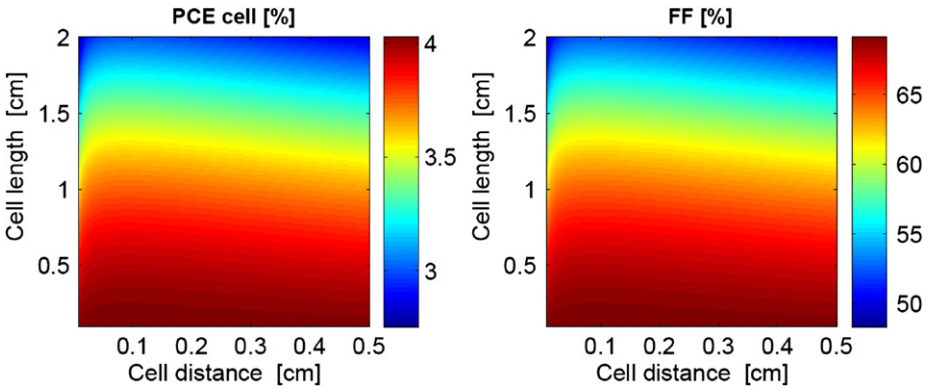

Fig. 11. Calculated power conversion efficiency (left) and fill factor (right) of solar cells with varying cell lengths and distances. As the performance is related to the active area of the solar cell alone, no area losses are taken into account.

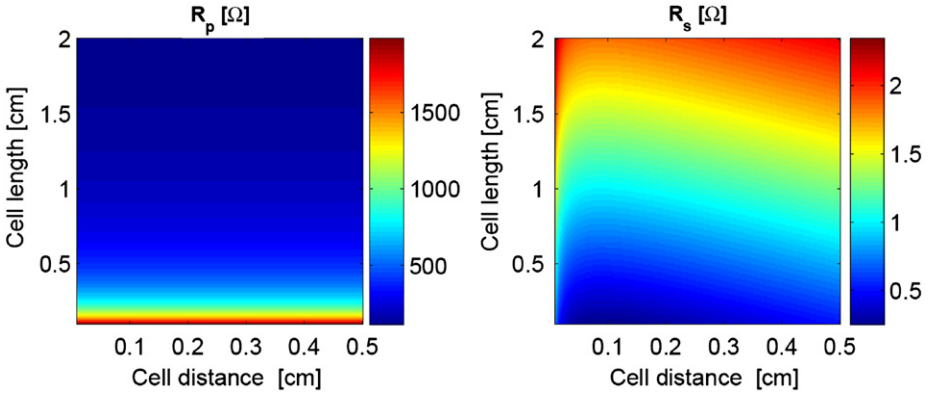

Fig. 12. Calculated parallel and series resistance for the periodically interconnected solar cell structure. Whereas R_P is a hyperbolic function of the cell length alone, R_S exhibits dependencies on both geometrical dimensions.

of solar cell distances. Furthermore it is evident that the aluminum resistance is rather negligible as compared to all the others, and the contact resistance has a major impact only for short contact lengths.

Based on the resistances and the respective currents passing them, the power dissipation at the maximum power point is calculated for each of the geometries. While one part of the photogenerated current has to pass all series resistances, another part–constituting the shunt current $I_{Rp,mpp}$ and being also controlled by the diode properties–is passing the parallel resistance, leading to individual resistive power losses. The total electric loss at the maximum power point is then obtained by adding the power losses due to all series resistances and the parallel resistance (compare with Fig. 14).

Finally the module power conversion efficiency, taking all geometric and electric losses at the maximum power point into account, is obtained. It is displayed for the set of different investigated semitransparent electrodes in Fig. 15. The influence arising from the area losses in solar modules is reflected by the loss in efficiency for longer cell distances. In general the region for maximum power conversion efficiency becomes more confined to shorter solar cell lengths, with the increasing sheet resistances. Increasing contact resistances lead to the requirement of longer contact pad lengths, which is reflected by the performance maximum occurring at slightly increased cell distances in case of PH 1000-based electrodes (compare with Fig. 15 right image).

From Fig. 15 it is evident that the module power conversion efficiency is dramatically reduced as compared to the cell. This effect

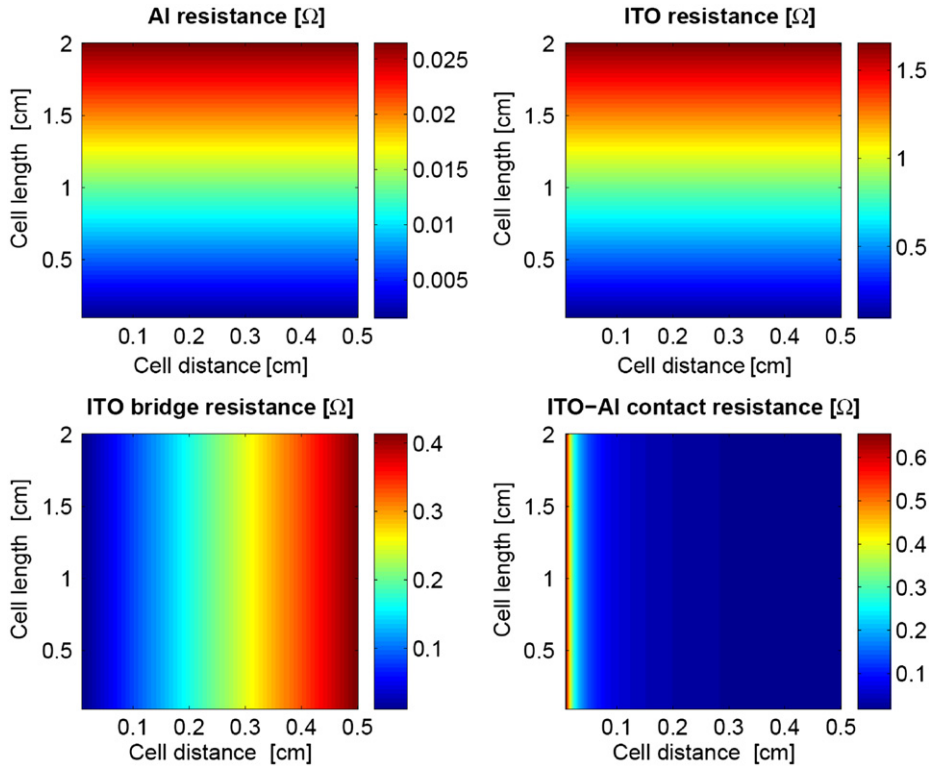

Fig. 13. Geometric dependencies of all individual series resistances involved in the current transport within the solar module. Major influences arise from the ITO resistance for long solar cell lengths and distances, and from the contact resistance for very short solar cell distances.

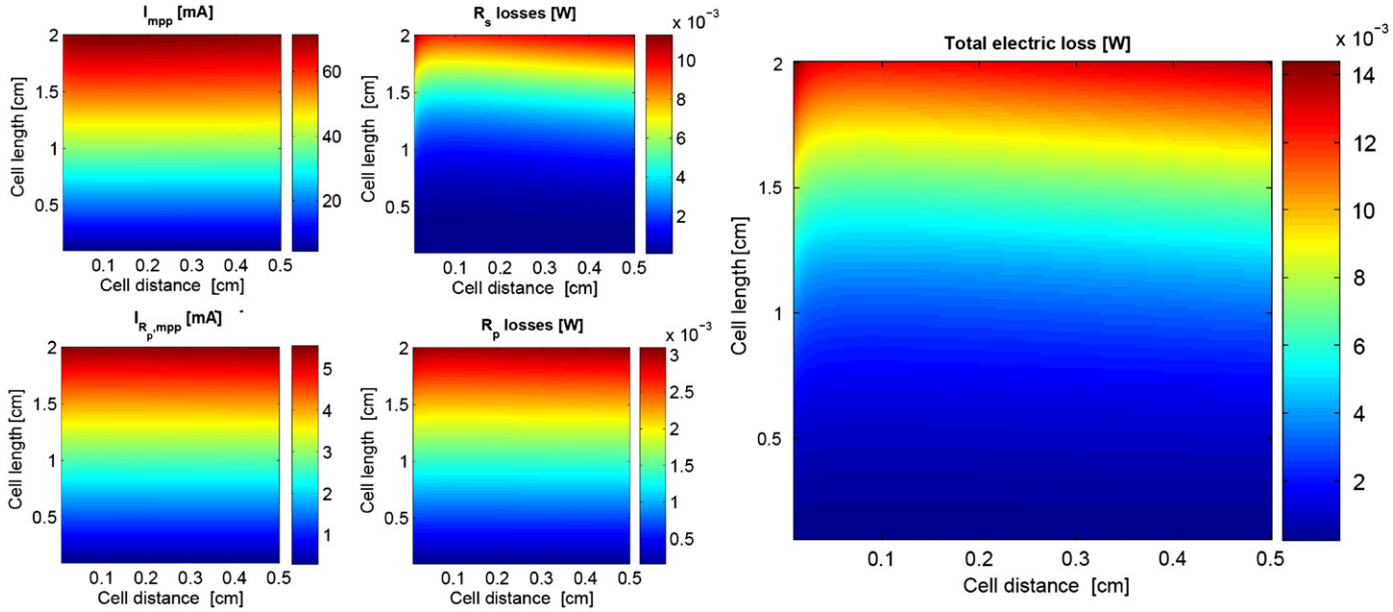

Fig. 14. Dissipative power losses at the maximum power point due to R_P and R_S are controlled by the shunting current $I_{Rp,mpp}$ and the part of the photocurrent passing through the series resistances. The distribution of the two components of the photocurrent flowing over the parallel and the series resistances is directly controlled by the diode properties.

is solely governed by the fact that for the solar module power conversion efficiency the whole substrate area is counting in, whereas for the solar cell only the device active area is taken into account. Whilst the geometrical losses become maximal for small solar cell lengths, the electric power losses increase mainly for longer solar cell lengths. This becomes strongly pronounced for the higher resistive ITO on PET and PH 1000 on PET (compare Fig. 15), therefore relatively small dimensions as compared to ITO on glass are required for reaching relatively high efficiencies. Due to the strong contribution from the large contact resistance in case of PH 1000 electrodes, the solar cell distance needs to be adjusted to slightly larger values than for the ITO-electrodes. However, even though relatively large sheet and contact resistances of course do limit the achievable power conversion efficiency in the case of the ITO-free layer stack, a considerable performance can be achieved for small solar cell lengths and distances. For example in the case of 0.5 cm solar cell length and 0.05 cm solar cell distance, which can be e.g. readily achieved by laser structuring of the interconnects, the ITO-glass system yields about

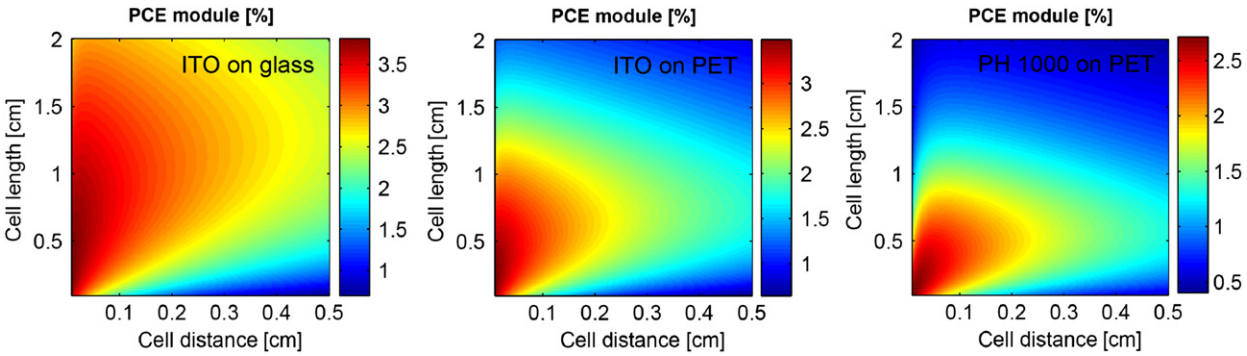

Fig. 15. Comparison of the module power conversion efficiency calculated for ITO on glass (left), ITO on PET (center) and PH 1000 on PET (right), for the resistance parameters shown in Tables 1 and 2. The maximum power conversion efficiency drops from above 3.5% to below 3.5% and then to below 2.5%, favouring smaller solar cell lengths but larger distances, for ITO on glass, ITO on PET and PH 1000 on PET, respectively.

3.5%, the ITO-PET system yields about 3.1% and the PH 1000-PET system yields 2.4% power conversion efficiency–and thus about two-third of the performance on glass with the given material system. Our calculations thus indicate that completely ITO-free solar modules can be commercially viable.

Furthermore, these calculations provide direct information about optimal device geometries to achieve the maximum performance attainable with an individual material system investigated. Finally, this combined experimental and numerical method yields fast and precise design rules for the appropriate device layout, once all materials and interface properties were determined. Thus this approach displays a powerful tool for the design of optimized solar modules.

5. Conclusion:

In conclusion we have shown that the combination of experimental methods, applied for determining sheet and contact resistances of electrodes, and numerical methods, applied for determining the electrical power dissipation losses, allows a thorough optimization of the solar cell and module device layout for the maximum electrical performance. Due to the use of a self-consistent calculation method computational errors arising from more simple models are successfully prevented. The combination of methods presented here can be understood as a recipe for maximizing the performance of a given material system. Any discrepancy between experimental results and the numerical evaluation clearly yields the optimization potential for each of the solar cell parameters.

Our results suggest that for higher resistive semitransparent electrodes, rather short solar cell lengths and short solar cell distances yield the highest module performance. This can be achieved e.g. by slot-dye coating in combination with laser ablation, or by some finely registered printing technology. Thus the simulation results can also be used to directly choose suitable deposition and structuring methods yielding the optimal geometry in solar module design.

Acknowledgments:

B.M. gratefully acknowledges financial support from the Thuringian Ministry of Culture.

References

[1] M. Grundmann, H. Frenzel, A. Lajn, M. Lorenz, F. Schein, H. von Wenckstern, Transparent semiconducting oxides: Materials and devices, Physica Status Solidi A 207 (2010) 1437–1449.
[2] S. Choi, W.J. Potscavage, B. Kippelen, Area-scaling of organic solar cells, Journal of Applied Physics 106 (2009) 054507-1–054507-10.
[3] B. Muhsin, J. Renz, K.H. Drue, G. Gobsch, H. Hoppe, Influence of polymer solar cell geometry on series resistance and device efficiency, Physica Status Solidi A 206 (2009) 2771–2774.
[4] M.A. Green, K. Emery, Y. Hishikawa, W. Warta, Solar cell efficiency tables (version 37), Progress in Photovoltaics 19 (2011) 84–92.
[5] R.F. Service, Outlook Brightens for Plastic Solar Cells, Science 332 (2011) 293.
[6] T.D. Nielsen, C. Cruickshank, S. Foged, J. Thorsen, F.C. Krebs, Business, market and intellectual property analysis of polymer solar cells, Solar Energy Materials and Solar Cells 94 (2010) 1553–1571.
[7] D. Gupta, M. Bag, K.S. Narayan, Area dependent efficiency of organic solar cells, Applied Physics Letters 93 (2008) 163301-1–163301-3.
[8] J.S. Yeo, J.M. Yun, S.S. Kim, D.Y. Kim, J. Kim, S.I. Na, Variations of cell performance in ITO-free organic solar cells with increasing cell areas, Semiconductor Science and Technology 26 (2011) 034010-1–034010-6.
[9] M.S. Kim, M.G. Kang, L.J. Guo, J. Kim, Choice of electrode geometry for accurate measurement of organic photovoltaic cell performance, Applied Physics Letters 92 (2008) 133301-1–133301-3.
[10] M.W. Rowell, M.D. McGehee, Transparent electrode requirements for thin film solar cell modules, Energy and Environmental Science 4 (2011) 131–134.
[11] F.C. Krebs, T. Tromholt, M. Jorgensen, Upscaling of polymer solar cell fabrication using full roll-to-roll processing, Nanoscale 2 (2010) 873–886.
[12] R. Rösch, B. Muhsin, M. Bärenklau, A. Schoonderbeek, G. Gobsch, L. Richter, R. Kling, D. Teckhaus and H. Hoppe, Towards Roll-To-Roll Processing of Flexible Polymer Solar Cell Modules, presented at: 24th EUPVSEC, Hamburg, Germany, p. 672-675.
[13] A. Schoonderbeek, M. Bärenklau, R. Rösch, D. Teckhaus, B. Muhsin, O. Haupt, H. Hoppe and U. Stute, Laser structuring for monolithic series connection of organic thin-film solar cells, presented at: 25th EUPVSEC, Valencia, Spain, p. 319-324.
[14] J. Meier, J. Spitznagel, U. Kroll, C. Bucher, S. Fay, T. Moriarty, A. Shah, Potential of amorphous and microcrystalline silicon solar cells, Thin Solid Films 451 (2004) 518–524.
[15] F. Kessler, D. Rudmann, Technological aspects of flexible CIGS solar cells and modules, Solar Energy 77 (2004) 685–695.
[16] J. Hermann, M. Benfarah, S. Bruneau, E. Axente, G. Coustillier, T. Itina, J.F. Guillemoles, P. Alloncle, Comparative investigation of solar cell thin film processing using nanosecond and femtosecond lasers, Journal of Physics D: Applied Physics 39 (2006) 453–460.
[17] B. Muhsin, J. Renz, K.H. Drue, G. Gobsch, H. Hoppe, Efficient polymer solar cell modules, Synthetic Metals 159 (2009) 2358–2361.
[18] T. Petsch, J. Haenel, M. Clair, B. Keiper and C. Scholz, Laser Processing of Organic Photovoltaic Cells with a Roll-To-Roll Manufacturing Process, Proceedings of the SPIE - The International Society for Optical Engineering p. 79210U (7 pp.) (2010).
[19] H. Hoppe, S. Shokhovets, G. Gobsch, Inverse relation between photocurrent and absorption layer thickness in polymer solar cells, Physica Status Solidi Rapid Research Letters 1 (2007) R40–R42.
[20] J.A. Renz, T. Keller, M. Schneider, S. Shokhovets, K.D. Jandt, G. Gobsch, H. Hoppe, Multiparametric optimization of polymer solar cells: A route to reproducible high efficiency, Solar Energy Materials and Solar Cells 93 (2009) 508–513.
[21] L.J. van der Pauw, A method of measuring the resistivity and hall coefficient on lamellae of arbitrary shape, Philips Technical Review 20 (1958/59) 220–224.
[22] W. Shockley, Report no. Al-TOR-64-207, Air Force Atomic Laboratory, Wright-Patterson Air Force Base, Ohio, 1964.